2014

Smear signature morphology of surface targets with arbitrary motion in spotlight synthetic aperture radar imagery

Garren, David Alan

Institution of Engineering and Technology

Garren, D.A., "Smear signature morphology of surface targets with arbitrary motion in spotlight synthetic aperture radar," IET Radar Sonar Navigation (2014), v.8, iss.5, pp. 435-448.

http://hdl.handle.net/10945/56207

Published in IET Radar, Sonar and Navigation
Received on 23rd May 2013
Revised on 6th July 2013
Accepted on 21st July 2013
doi: 10.1049/iet-rsn.2013.0169

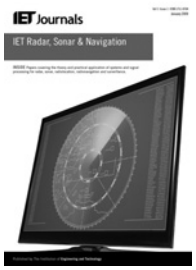

ISSN 1751-8784

Smear signature morphology of surface targets with arbitrary motion in spotlight synthetic aperture radar imagery

David Alan Garren

Department of Electrical and Computer Engineering, Naval Postgraduate School, Monterey, California 93943, USA
E-mail: dagarren@nps.edu

Abstract: This study develops a methodology for analytically predicting the detailed smear signature morphology of surface targets with arbitrary motion in spotlight synthetic aperture radar (SAR) imagery. The radar sensor is assumed to move with constant speed and heading on a level flight path with broadside imaging geometry. Cases of uniform target motion exhibit morphology of simply curved smear shapes, as has been reported previously. However, the present analysis shows that non-uniform target motion can cause complicated smear shapes in spotlight SAR imagery. Specifically, the method of stationary phase is applied to local subaperture SAR images to yield analytic non-parametric expressions for the morphology of smear signatures within spotlight SAR imagery for surface targets with arbitrary motion trajectories. This predictive capability offers the potential of extracting some characteristics of true target motion based upon the induced SAR smear signatures alone.

1 Introduction

It is well known that moving targets cause smeared signatures when imaged using synthetic aperture radar (SAR). The majority of the smearing lies in the radar cross-range direction of the SAR imagery, regardless of the particular SAR imaging mode used. Raney [1] has described much of the basic phenomenology of moving target motion effects in SAR imagery, including cross-range offset and defocus effects. In addition, Perry *et al.* [2] have developed a method for refocusing the smeared signatures of moving targets under the assumption that the target motion smearing lies in the radar cross-range direction. Furthermore, Fienup [3] has developed a shear averaging algorithm used to perform automatic detection and focusing of moving target smears in SAR imagery under the assumption that the motion-induced smearing lies in the radar cross-range direction. Cristallini *et al.* [4] have applied chirp scaling algorithms (CSA) to develop an efficient method for detecting and focusing moving targets in SAR imagery under similar assumptions of target cross-range smearing. These techniques assume that the target motion-induced smearing occurs in the cross-range direction alone.

Other researchers have investigated the effects of moving targets in SAR imagery. Specifically, the objectives of target motion analysis, moving target detection and moving target imaging are interrelated, as any attempt to detect moving targets in SAR via imaging will require a detailed understanding of the defocus smearing effects induced by target motion in SAR imagery. For example, Jakowatz *et al.* [5] have investigated the properties of constant velocity targets in SAR imagery. In addition, Rigling [6] has developed a method for focusing rotating targets that are rotating via an image entropy optimisation process. Vu *et al.* [7] have investigated methods for focusing targets in ultra-wideband SAR, wherein target migration effects are especially important. Stojanovic and Karl [8] have developed a method for imaging moving targets in SAR through the use of an overcomplete dictionary. Leducq *et al.* [9] have developed a matching pursuit method for analysing moving targets in polarimetric SAR images. Fasih *et al.* [10] have examined the effects of random motion components of moving targets in SAR imagery. Zhu *et al.* [11] developed a method for focusing ground moving targets in SAR imagery without prior knowledge of the motion parameters. Cheney and Borden [12] have examined the imaging of moving targets in spotlight SAR through the use of almost arbitrary waveforms. Xu *et al.* [13] have demonstrated that a moving target SAR signature can become split into two signatures. Yake *et al.* [14] have developed a method for focusing moving targets in SAR imagery for cases in which there is significant range walk. Li *et al.* [15] have investigated the effects of micromotion in SAR and ground moving target indication radar. Deng *et al.* [16] utilise a power series expansion in order to examine the effects in SAR imagery of higher-order target motions, such as accelerations, jerks or micromotions.

Other research into moving targets in SAR imagery also includes the following works. DiPietro *et al.* [17] have investigated the use of a matched filtering technique for detecting moving targets in long-dwell SAR. Barbarossa *et al.* [18–20] have developed methods for detecting and

focusing moving targets in SAR imagery based upon the use of the Wigner–Ville distribution and maximum-likelihood theory. Kirscht [21] has developed methods for estimating the kinematics parameters of a moving target in SAR imagery by computing a sequence of multi-look SAR images. Dias and Marques [22] have developed a method for detecting moving targets in stripmap SAR imagery and for estimating their corresponding motion parameters, assuming constant velocity. Marques and Dias [23] have developed a methodology for estimating the kinematics motion parameters of moving targets using only a single SAR sensor.

Jao [24] has investigated the phenomenology that a moving target signature in stripmap-mode SAR imagery has a curved bowing signature in the down-range direction. The bowing of moving target signatures is related to the range migration effects that occur prior to the focusing of stationary scenes. Such range migration effects can be compensated through the use of the Stolt mapping or interpolation techniques [25]. These techniques were originally developed for seismic data but have found useful application in the focusing of stationary scenes for low frequency radar data via the range migration algorithm (RMA). RMA ingests unfocused imagery wherein stationary scattering centres appear as defocused arcs and then focuses these arcs to be points. Conventional focusing algorithms do not compensate for this residual range migration and result in imagery containing residual defocus at lower radar frequencies. Recently, Rahman [26] has investigated the application of the RMA to the focusing of moving targets which bear the characteristic curvature morphology [24].

Recent work has suggested that moving targets typically exhibit gently curved profiles in SAR imagery. These morphological shapes reveal smearing that lies primarily in the cross-range direction, with a slight bowing that is either concave up or concave down. This result applies for any target that moves with constant velocity [24]. An analytic explanation follows from a power series expansion analysis of the various phase error contributions, as has been presented in numerous works [7, 24, 27–30]. There appears to be a common perception that all moving target signatures are defocused with shapes of approximate parabolas, or more specifically, elliptic or hyperbolic curves. In fact, analyses [27–30] that rely upon power series expansions of the phase error terms seem to support this perception.

However, recent investigation of particular non-uniform target motion has resulted in non-typical signature morphology [31] but did not provide an understanding of the signature shapes. The unique contribution of the present analysis herein is that it does provide analytic closed-form equations for explicitly predicting the morphology of moving target smears. Specifically, the present analysis investigates the phase error applied to subaperture SAR images and yields more general expressions for SAR moving target signatures which are not constrained to have elliptic or hyperbolic form. In particular, the permitted surface target motion in the present analysis herein is based upon the use of subapertures, so that this target motion is completely arbitrary and fully non-parametric. That is, the central time value of each subaperture corresponds to the target motion at that particular time, thus enabling SAR phenomenology analysis for arbitrary target trajectories. This analysis can be shown to yield complicated smear signatures for some types of target motion. In summary, the use of subapertures enables an analysis of spotlight SAR signatures corresponding to arbitrary target motion trajectories, not just constant velocity targets, in a concise and practical framework. Previous attempts to analyse higher-order target motion via higher order power series expansions [15, 16, 27] have found that the analyses quickly become quite cumbersome and challenging in implementation when applied to complex target motions that are non-periodic and do not exhibit constant acceleration.

Specifically, the current paper examines the morphology of smear signatures for arbitrarily moving surface targets for spotlight-mode SAR, which is a radar imaging mode [32–36] used to maximise image resolution at the expense of area coverage rate. The current analysis presented herein applies for all different types of spotlight SAR image formation algorithms, including, but not limited to, the polar formatting algorithm (PFA), RMA and CSA. However, the current analysis described herein is limited to spotlight-mode SAR, since non-trivial modifications to the analysis would be required in order to address stripmap SAR. Thus, an analysis of target motion effects for stripmap SAR is reserved for future work.

The fundamental analytics in the present paper is based upon the prediction of moving target signature within SAR subaperture images. Numerous researches have utilised subaperture SAR images for various purposes. One of the earliest works in the use of subapertures, or equivalently, subarrays, was developed by Perry *et al.* [37]. Subaperture images can reveal information about the full-aperture SAR image morphology. For example, each moving target smear in a subaperture image traces a portion of the larger smear in the full-aperture image, which is because of the same moving target. Zhang *et al.* [38] have applied subaperture images in order to filter speckle from SAR images. Soumekh [39, 40] has divided a full-aperture stripmap SAR data set into a number of overlapping subaperture images in order to form high resolution spotlight SAR images. Ferro-Famil *et al.* [41] has applied subaperture analysis that incorporates a deconvolution technique for polarimetric data. Greidanus [42] has studied SAR signatures of ships with regards to their effects in subaperture images.

The next section defines the overall geometry and coordinates that are used in this analysis. Section 3 provides the model used in computing the radar signal information based upon a particular set of platform and radar collection parameters. Section 4 develops a power series analysis that is used to compute the moving target signatures within the subaperture images. Section 5 considers specific examples for the target trajectory profiles in order to understand the resulting signature effects in the subaperture images. Section 6 compares the specific examples of target trajectories with those obtained from numeric computations. The conclusions are presented in the final section.

2 Geometry and coordinates

This analysis begins with the definition of the coordinates for the radar and the scene to be imaged. Define x, y, z to be a spatial Cartesian coordinate system, with the $z = 0$ coordinate surface defining the target ground plane with x, y, $z = 0$, 0, 0. This coordinate origin is equal to the ground reference point (GRP), or equivalently, the aim-point of the radar mainbeam for the spotlight SAR collection. The coordinate z increases with increasing elevation above the ground plane. The positive x coordinate is defined to correspond with increasing ground range from the radar. Finally, the y coordinate lies in the ground cross-range

doi: 10.1049/iet-rsn.2013.0169

direction, so that x, y, z forms a right-handed coordinate system.

Assume that the radar transmits and receives radar waveforms for a total time of T_0. Also, define t to be the slow-time coordinate for the radar waveform transmission and reception. Without loss in generality, define $t=0$ to be the mid-point in time of the SAR collection. Thus, the slow-time t is assumed to vary between $-T_0/2$ and $T_0/2$ over the full-synthetic aperture of the collection. Also, the ground down-range x coordinate lies along the projected line in the ground plane from the radar aperture centre-point at $t=0$ to the GRP. The ground cross-range coordinate y lies mutually perpendicular to the x and z coordinates.

It is useful to consider the special case of an idealised point target that moves within the ground plane of $z=0$ according to the analytic trajectory functions $\alpha(t)$, $\beta(t)$, in the ground down-range and ground cross-range directions, x and y, respectively. Thus, this target motion is assumed to have the following general form

$$x = \alpha(t) \tag{1}$$

$$y = \beta(t) \tag{2}$$

For the purposes of this analysis, the temporal functions $\alpha(t)$, $\beta(t)$ are assumed to be analytic functions of the SAR collection slow-time t. The assumed analytic properties of these two functions enable the application of power series analysis in order to facilitate an understanding of the various contributions to the target motion signature. This analytic assumption is reasonable, since the present analysis models the SAR signatures of physical moving targets with non-zero inertia. This non-zero inertia serves to inhibit instantaneous changes in any of the primary target kinematics properties of the target position, velocity or acceleration etc.

In order to perform the required analytic calculations, it is necessary to develop a viable parameterisation of a radar platform trajectory corresponding to a straight and level flight path with constant speed and a broadside radar imaging geometry. One possible parameterisation of this standard spotlight SAR imaging platform is the following in terms of a ground plane Cartesian coordinate system x, y, z

$$X(t) = -X_0 \tag{3}$$

$$Y(t) = \pm V_0 t \tag{4}$$

$$Z(t) = Z_0 \tag{5}$$

with V_0 equal to the speed of the radar platform, with X_0 equal to the radar ground range relative to the synthetic aperture centre and Z_0 equal to the radar elevation above the ground plane. Recall that the origin of the global Cartesian coordinates is selected to be the fixed aim-point on the ground to which the radar mainbeam is pointed during this spotlight SAR image collection interval. This aim-point of the radar is also referred to as the GRP. The positive sign in (4) denotes radar motion in the $+y$ direction, and the minus sign defines movement in the $-y$ direction. From (3)–(5) above, it is convenient to define the azimuth and elevation angles, respectively, of the radar platform relative to the GRP via

$$\theta(t) \equiv \arctan\left(\frac{Y(t)}{X(t)}\right) \tag{6}$$

$$\varphi(t) \equiv \arctan\left(\frac{Z(t)}{\sqrt{X^2(t)+Y^2(t)}}\right) \tag{7}$$

3 Radar measurements

This analysis requires the mathematical framework for predicting the frequency domain SAR data based upon assumed geometries for the radar platform and the various surface mobile targets within the imaged scene. To do so, one should begin this characterisation in terms of variables that are convenient for ingesting measured SAR data. To perform this calculation, begin with the following model of the down-converted, frequency-domain SAR measurement data in the original 'polar' format

$$\tilde{G}\left(f_{m'}, t_{n'}\right) = \Sigma_i \sigma_i \exp\left(-j2\pi\Delta R_i(t_{n'})2f_{m'}/c\right) \tag{8}$$

In this equation, the path difference relative to the GRP is defined by

$$\Delta R_i\left(t_{n'}\right) \equiv R_i\left(\theta\left(t_{n'}\right), \varphi\left(t_{n'}\right)\right) - R_0\left(\theta\left(t_{n'}\right), \varphi\left(t_{n'}\right)\right) \tag{9}$$

In (8), the complex-valued measured quantities $\tilde{G}$ give both the real (i.e. in phase) and imaginary (i.e. quadrature) components of the sub-band centred on frequency sample value $f_{m'}$ corresponding to the radar waveform received at slow-time sample value $t_{n'}$. The constant c is the speed of light, and $j=\sqrt{-1}$ is the imaginary constant. The factor of 2 in the argument of the exponential function accounts for the two-way propagation of the radar. In (8), the summation over i applies to extended targets having multiple scattering centres. In (9), the quantity $R_i(\theta(t_{n'}), \varphi(t_{n'}))$ is equal to the range or distance from the radar platform for the radar waveform received at slow-time $t_{n'}$ to the ith scattering centre characterised by the complex-valued reflectivity σ_i

$$R_i\left(\theta\left(t_{n'}\right), \varphi\left(t_{n'}\right)\right) = \sqrt{\left\{X(t_{n'}) - \alpha(t_{n'})\right\}^2 + \left\{Y(t_{n'}) - \beta(t_{n'})\right\}^2 + \left\{Z(t_{n'})\right\}^2} \tag{10}$$

Likewise, $R_0(\theta(t_{n'}), \varphi(t_{n'}))$ equals the range from the radar platform to the spotlight-SAR GRP lying at the x, y, $z=0$, 0, 0 coordinate origin, that is

$$R_0\left(\theta\left(t_{n'}\right), \varphi\left(t_{n'}\right)\right) = \sqrt{\left\{X(t_{n'})\right\}^2 + \left\{Y(t_{n'})\right\}^2 + \left\{Z(t_{n'})\right\}^2} \tag{11}$$

In the idealised point scattering centre example presented in this analysis, the summation of (8) has the single term of a single idealised point target scattering centre, with $i=1$.

It should be clarified that the R_0 in (9) gives the constant phase reference of the GRP used in spotlight SAR image formation. That is, (9) applies only to all types of spotlight SAR image formation algorithms, including, but not limited to, PFA, RMA and CSA. A similar analysis applied to stripmap SAR is reserved for future work.

The target migration signature analysis developed herein is applied specifically to spotlight SAR image data in the ground plane of $z = 0$. In order to obtain such ground plane image data, it is convenient to define the following functions that delineate the ground range and the ground cross-range components of the spatial frequency, respectively

$$\xi_m(f_{m'}, t_{n'}) \equiv \frac{2f_{m'}}{c}\cos\left(\theta(t_{n'})\right)\cos\left(\varphi(t_{n'})\right) \tag{12}$$

$$\eta_m(f_{m'}, t_{n'}) \equiv \frac{2f_{m'}}{c}\cos\left(\theta(t_{n'})\right)\sin(\varphi(t_{n'})) \tag{13}$$

Equations (12) and (13) are simply the direction cosine projections of the original polar sample data, with the spatial frequency spherical polar radius $2f'_m/c$, the azimuth angle $\theta(t_{n'})$, and the elevation angle $\varphi(t_{n'})$. A polar-to-rectangle sampling operation [35], or a similar procedure, must be applied to obtain the desired Cartesian-sampled data, that is

$$\tilde{G}(f_{m'}, t_{n'}) \underset{\text{pol}}{\rightarrow} G(\xi_m, \eta_n) \tag{14}$$

here, $G(\xi_m, \eta_n)$ denotes the complex-valued frequency-domain Cartesian data in terms of M discrete resampled values of the ground range spatial frequency ξ_m and N discrete resampled values of the ground cross-range spatial frequency η_n. From these data, a two-dimensional (2D) discrete Fourier transform (DFT) yields the desired spotlight SAR image

$$G(\xi_m, \eta_n) \underset{2D\ \text{DFT}}{\leftrightarrow} b(x_k, y_\ell) \tag{15}$$

In addition, it is assumed that both sensor motion compensation and autofocus processing have been applied previously to the data in order to obtain well-focused imagery of the stationary scene content.

The computation of the subaperture SAR images can be performed by evaluating the following expression

$$b_s(x, y) = \int_{\xi_0-\Delta\xi/2}^{\xi_0+\Delta\xi/2} \mathrm{d}\xi \int_{\eta_s-\Delta\eta/2}^{\eta_s+\Delta\eta/2} \mathrm{d}\eta \tilde{G}(\xi, \eta) \exp(\mathrm{j}2\pi(x\xi + y\eta)) \tag{16}$$

with s equal to the subaperture index, ξ_0 equal to the central value of the ground range spatial frequency, and η_s equal to the central value of the ground cross-range spatial frequency corresponding to subaperture s. A predictive evaluation of (16) requires knowledge of the value of the slow-time t for every sample value of the spatial frequency coordinates (ξ, η). In order to perform this calculation, it is useful to apply (3)–(5) for the parametric specification of the radar platform trajectory.

The azimuthal angle θ in the spatial domain of the ground plane coordinate system x, y, z is identical to that for the corresponding spatial frequency coordinates ξ, η, ζ, with ζ equal to the spatial frequency in the elevation direction. Thus, the tangent of the azimuthal angle can be expressed in the dual form

$$\tan(\theta) = \frac{Y(t)}{X(t)} = \frac{\eta}{\xi} \tag{17}$$

Substituting (3)–(5) for the parametric specification of the radar platform trajectory in time gives

$$\mp\frac{V_0 t}{X_0} = \frac{\eta}{\xi} \tag{18}$$

Equation (17) can be used to solve for the slow-time t in terms of the spatial frequency coordinates (ξ, η) and the platform geometrical variables via

$$t(\xi, \eta) = \kappa_0 \frac{\eta}{\xi} \tag{19}$$

in terms of a temporal constant defined by

$$\kappa_0 \equiv \mp\frac{X_0}{V_0} \tag{20}$$

Equation (26) indicates that the mean value of slow-time t for a given subaperture s is given by

$$t = \tau_s \equiv \kappa_0 \frac{\eta_s}{\xi_0} \tag{21}$$

4 Power series expansion

The overall goal of this analysis is to predict the mean position of the smear signature location in a particular subaperture image s centred about a time of $t = \tau_s$. Thus, it is useful to find an approximate expression for the target motion for a small subaperture corresponding to a time interval centered about $t = \tau_s$. It is valuable to perform a power series expansion of the target motion functions $\alpha(t)$, $\beta(t)$ about the subaperture mean time of $t = \tau_s$, giving local power series expressions for the target motion functions as defined by $\alpha_s(t)$, $\beta_s(t)$, that is

$$\alpha(t) = \alpha_s(t) \equiv \sum_{n=0}^{\infty} \frac{1}{n!}\mu_n(\tau_s)\{t - \tau_s\}^n \tag{22}$$

$$\beta(t) = \beta_s(t) \equiv \sum_{n=0}^{\infty} \frac{1}{n!}\nu_n(\tau_s)\{t - \tau_s\}^n \tag{23}$$

In (22) and (23), the expansion coefficient functions $\mu_0(\tau_s)$, $\nu_0(\tau_s)$ give instantaneous target position, which is constrained to move within the ground plane of $z = 0$, evaluated at the mean subaperture time τ_s. Likewise, the expansion coefficient functions $\mu_1(\tau_s)$, $\nu_1(\tau_s)$ give the instantaneous target velocity, and the expansion coefficient functions $\mu_2(\tau_s)$, $\nu_2(\tau_s)$ give the instantaneous target acceleration, both contained within the ground plane of $z = 0$ and evaluated at the mean subaperture time τ_s. The first element of each of these kinematics quantities lies in the ground down-range direction $\hat{\boldsymbol{x}}$, and the second element of each lies in the ground cross-range direction $\hat{\boldsymbol{y}}$. The third unit vector $\hat{\boldsymbol{z}}$ is normal to the ground plane and increases with elevation above the ground. These ground-plane unit vectors, $\{\hat{\boldsymbol{x}}, \hat{\boldsymbol{y}}, \hat{\boldsymbol{z}}\}$, are fixed in space and do not move or rotate as a function of the mean subaperture time τ_s.

The evaluation of the subaperture images $b_s(x, y)$ in (16) continues by reworking the integral in terms of 'centred'

doi: 10.1049/iet-rsn.2013.0169

spatial frequencies defined by

$$\tilde{\xi} = \xi - \xi_0 \tag{24}$$

$$\tilde{\eta} = \eta - \eta_s \tag{25}$$

Thus, this expression for the slow-time t in (19) can be expressed in the form

$$t(\tilde{\xi}, \tilde{\eta}, \eta_s) = \kappa_0 \frac{\eta_s + \tilde{\eta}_s}{\xi_0 + \tilde{\xi}} \tag{26}$$

in order to compute subaperture images corresponding to some particular target motion. In addition, (16) becomes

$$b_s(x, y) = \sigma_0 \int_{-\Delta\xi/2}^{\Delta\xi/2} \mathrm{d}\tilde{\xi} \int_{-\Delta\eta/2}^{\Delta\eta/2} \mathrm{d}\tilde{\eta} \exp\left(\mathrm{j}2\pi\Omega(x, y, \tilde{\xi}, \tilde{\eta}, \eta_s)\right) \tag{27}$$

in terms of the phase function $\Omega(x, y, \tilde{\xi}, \tilde{\eta}, \eta_s)$ defined by

$$\Omega(x, y, \tilde{\xi}, \tilde{\eta}, \eta_s) = \left[x - \alpha_s(t(\tilde{\xi}, \tilde{\eta}, \eta_s))\right]\left[\xi_0 + \tilde{\xi}\right] + \left[y - \beta_s(t(\tilde{\xi}, \tilde{\eta}, \eta_s))\right]\left[\eta_s + \tilde{\eta}\right] \tag{28}$$

To further understand moving target signatures in spotlight SAR imagery, it is useful to perform a power series expansion of the phase function $\Omega(x, y, \tilde{\xi}, \tilde{\eta}, \eta_s)$ of (28) in terms of three dimensionless parameters that are typically small for narrow-band SAR image formation

$$\epsilon_x \equiv \frac{\tilde{\xi}}{\xi_0} \tag{29}$$

$$\epsilon_y \equiv \frac{\tilde{\eta}}{\xi_0} \tag{30}$$

$$\epsilon_s \equiv \frac{\eta_s}{\xi_0} \tag{31}$$

Further analysis of (27) requires evaluation of the phase in (28) through at least third order in the 3D Taylor series expansion in terms of ε_x, ε_y, ε_s to assess the signature characteristics of moving scattering centres within the SAR imagery. The linear phase terms will be seen to affect the drift of each mover with regard to subaperture, and the quadratic terms will be seen to affect the focus of each mover. A third-order expansion is required, since it is necessary to evaluate these signature characteristics for subaperture images, which require retention of terms that are linear in ϵ_s in the power series expansion of the phase function.

To enable the power series expansion of the phase function of (28), first note that the mean subaperture time τ_s has the form

$$\tau_s = \kappa_0 \epsilon_s \tag{32}$$

Also, the slow-time t and the relative subaperture slow-time $t - \tau_s$ have the following forms in terms of the power series expansion variables

$$t = \kappa_0 \frac{\epsilon_s + \epsilon_y}{1 + \epsilon_x} \tag{33}$$

$$t - \tau_s = \kappa_0 \frac{\epsilon_s + \epsilon_y}{1 + \epsilon_x} - \kappa_0 \epsilon_s \tag{34}$$

The overall analysis strategy of matching like powers in the power series expansion requires that it is only necessary to perform a power series expansion in terms of the expression $(1 + \epsilon_x)^{-1} = \sum_{n=0}^{\infty} \epsilon_x^n$, which leads to the following form for (34)

$$\frac{t - \tau_s}{\kappa_0} = \left\{\epsilon_s + \epsilon_y\right\}\left\{1 - \epsilon_x + \epsilon_x^2 - \epsilon_x^3 + \cdots\right\} \tag{35}$$

Retaining only terms through third order in ε_x, ε_y, ε_s leads to the following forms for the first, second and third powers of $t - \tau_s$

$$\frac{t - \tau_s}{\kappa_0} = \epsilon_y - \left\{\epsilon_s + \epsilon_y\right\}\epsilon_x + \left\{\epsilon_s + \epsilon_y\right\}\epsilon_x^2 - \cdots \tag{36}$$

$$\left\{\frac{t - \tau_s}{\kappa_0}\right\}^2 = \epsilon_y^2 - 2\epsilon_s\epsilon_x\epsilon_y - 2\epsilon_x\epsilon_y^2 + \cdots \tag{37}$$

$$\left\{\frac{t - \tau_s}{\kappa_0}\right\}^3 = \epsilon_y^3 + \cdots \tag{38}$$

Inserting (36)–(38) into (22) and (23) yields the following forms for the subaperture target motion functions

$$\begin{aligned}\alpha_s\left(t\left(\epsilon_x, \epsilon_y, \epsilon_s\right)\right) = {} & \mu_0(\tau_s) - \kappa_0\mu_1(\tau_s)\epsilon_s\epsilon_x + \kappa_0\mu_1(\tau_s)\epsilon_y \\ & + \kappa_0\mu_1(\tau_s)\epsilon_s\epsilon_x^2 \\ & - \left\{\kappa_0\mu_1(\tau_s) + \kappa_0^2\mu_2(\tau_s)\epsilon_s\right\}\epsilon_x\epsilon_y \\ & + \frac{1}{2}\kappa_0^2\mu_2(\tau_s)\epsilon_y^2 + \kappa_0\mu_1(\tau_s)\epsilon_x^2\epsilon_y \\ & - \kappa_0^2\mu_2(\tau_s)\epsilon_x\epsilon_y^2 + \frac{1}{6}\kappa_0^3\mu_3(\tau_s)\epsilon_y^3 + \cdots\end{aligned} \tag{39}$$

$$\begin{aligned}\beta_s(t(\epsilon_x, \epsilon_y, \epsilon_s)) = {} & \nu_0(\tau_s) - \kappa_0\nu_1(\tau_s)\epsilon_s\epsilon_x \\ & + \kappa_0\nu_1(\tau_s)\epsilon_y - \kappa_0\nu_1(\tau_s)\epsilon_x\epsilon_y + \frac{1}{2}\kappa_0^2\nu_2(\tau_s)\epsilon_y^2 + \cdots\end{aligned} \tag{40}$$

Equations (39) and (40) are inserted into (28) through third order in $\{\epsilon_x, \epsilon_y, \epsilon_s\}$. Thus, β_s in (40) is expanded through only second order because of the factor of $\eta_s + \eta_y$ in (28). The resulting phase function has the following form

through third order in $\{\epsilon_x, \epsilon_y, \epsilon_s\}$

$$\begin{aligned}
&\frac{\Omega(x, y, \epsilon_x, \epsilon_y, \epsilon_s)}{\xi_0} \\
&= \{[x - \mu_0(\tau_s)] + \epsilon_s[y - \nu_0(\tau_s)]\} \\
&\quad + \epsilon_x\{[x - \mu_0(\tau_s)] + \varepsilon_s\kappa_0\mu_1(\tau_s) + \epsilon_s^2\kappa_0\nu_1(\tau_s)\} \\
&\quad + \epsilon_y\{y - \nu_0(\tau_s) - \kappa_0\mu_1(\tau_s) - \epsilon_s\kappa_0\nu_1(\tau_s)\} \\
&\quad + \epsilon_x\epsilon_y\epsilon_s\{2\kappa_0\nu_1(\tau_s) + \kappa_0^2\mu_2(\tau_s)\} \\
&\quad - \epsilon_y^2\left\{\left[\kappa_0\nu_1(\tau_s) + \frac{1}{2}\kappa_0^2\mu_2(\tau_s)\right] + \epsilon_s\frac{1}{2}\kappa_0^2\nu_2(\tau_s)\right\} \\
&\quad + \epsilon_x\epsilon_y^2\left\{\kappa_0\nu_1(\tau_s) + \frac{1}{2}\kappa_0^2\mu_2(\tau_s)\right\} \\
&\quad - \epsilon_y^3\left\{\frac{1}{2}\kappa_0^2\nu_2(\tau_s) + \frac{1}{6}\kappa_0^3\mu_3(\tau_s)\right\}
\end{aligned} \tag{41}$$

Analysis of the subaperture smear signatures is facilitated by inserting the phase function $\Omega(x, y, \epsilon_x, \epsilon_y, \epsilon_s)$ into (27) for $b_s(x, y)$. First notice that the following factor can be pulled outside of the integral in (27) and is therefore an irrelevant complex constant

$$\lambda_0(x, y, \epsilon_s) = \exp(\mathrm{j}2\pi\xi_0\{[x - \mu_0(\tau_s)] + \epsilon_s[y - \nu_0(\tau_s)]\}) \tag{42}$$

It is desirable to find numeric expressions for the central or peak location of the smear signatures within each of the subaperture images. By the method of stationary phase, the integral in $b_s(x, y)$ has a maximum value when the coefficients of the dominant phase terms in $\Omega\left(x, y, \epsilon_x, \epsilon_y, \epsilon_s\right)$ are set equal to zero. Owing to the power series expansion of $\Omega\left(x, y, \epsilon_x, \epsilon_y, \epsilon_s\right)$, the dominant order terms that remain within the integral for $b_s(x, y)$ after the constant $\lambda(x, y, \epsilon_s)$ has been extracted are terms that are linear, that is, the ϵ_x and ϵ_y terms. Thus, the application of the method of stationary phase requires that the coefficients of ε_x and ε_y both be set equal to zero independently in order to find constraints on the location of the intensity peak in the smear signature location. An understanding of this concept follows since a zero value for the ε_x and ε_y coefficients implies that each of the complex terms in the summation for $b_s(x, y)$ is approximately unity, neglecting the residual effects of the second and higher order terms in $\{\epsilon_x, \epsilon_y\epsilon_s\}$ within the phase function. That is, a large summation of terms that are all approximately unity will give a maximum in the magnitude within the subaperture image $b_s(x, y)$.

Thus, the method of stationary phase implies that the central position of a moving target signature smear for a subaperture with mean time τ_s is obtained by setting the dominant linear order terms of ϵ_x term and ϵ_y term equal to zero in (42), yielding the following smear trajectory

$$x(\tau_s) = \mu_0(\tau_s) - \epsilon_s\kappa_0\mu_1(\tau_s) - \epsilon_s^2\kappa_0\nu_1(\tau_s) \tag{43}$$

$$y(\tau_s) = \nu_0(\tau_s) + \kappa_0\mu_1(\tau_s) + \varepsilon_s\kappa_0\nu_1(\tau_s) \tag{44}$$

Equations (43) and (44) specify the spatial location $\{x, y\}$ within the maximum magnitude of the moving target smear signature within the subaperture image $b_s(x, y)$. In this manner, a subaperture characterised by a central time of τ_s enables the evaluation of the contribution to the smear signature corresponding to the arbitrary target motion evaluated at this same time τ_s. Thus, the generic use of subapertures directly gives the predicted smear signature for a surface moving target executing arbitrary motion.

The reader should notice that $\{\mu_0(\tau_s), \nu_0(\tau_s), \mu_1(\tau_s), \nu_1(\tau_s)\}$ can be selected according to any arbitrary target motion. That is, these four functions need only satisfy the self-consistency between the components of the position $\{\mu_0(\tau_s), \nu_0(\tau_s)\}$ and the corresponding components of the velocity $\mu_1(\tau_s)$, $\nu_1(\tau_s)\}$. Thus, the target need not be parameterised or approximated as having constant velocity or constant acceleration. Instead, arbitrary non-parametric representations of a moving target can be applied in (43) and (44).

The basic condition for the necessity of this 2D smearing analysis is that the smearing must cover an extent in the down-range direction that exceeds a single pixel cell in the down-range direction. This constraint depends quite generally upon the radar collection parameters as well as the details of the target motion characteristics, as given by (43) for the target signature excursion in the down-range direction. Specifically, the 2D smearing analysis discussed herein is required for cases in which the full signature excursion of the down-range signature $x(\tau_s)$ in (43) exceeds the down-range resolution δx. If the full signature excursion of the down-range component $x(\tau_s)$ in (43) is less the down-range resolution δx, then a standard 1D analysis is sufficient. More will be presented on this issue in the next subsection.

5 Specific examples

5.1 Constant velocity targets

The moving target smear trajectory of (43) and (44) can be used to determine the expected subaperture smear characteristics within subaperture spotlight SAR images for various classes of physical target trajectories. Then, these subaperture smear characteristics can be used to surmise the morphology of the target smear within a full aperture of a spotlight SAR image. The initial special case to be examined is that of a constant velocity point target, characterised by

$$\alpha(t) = \bar{\alpha}_0 + \bar{\alpha}_1 t \tag{45}$$

$$\beta(t) = \bar{\beta}_0 + \bar{\beta}_1 t \tag{46}$$

with $\bar{\alpha}_0$, $\bar{\alpha}_1$, $\bar{\beta}_0$ and $\bar{\beta}_1$ all constant parameters.

The nth order derivatives of true target trajectory functions, as given by (45) and (46) for a constant velocity target, yield expressions for the coefficient expansion functions used in (22) and (23), that is

$$\mu_n(\tau_s) = \frac{d^n\alpha(t)}{\mathrm{d}t^n}|_{t=\tau_s} \tag{47}$$

$$\nu_n(\tau_s) = \frac{d^n\beta(t)}{dt^n}|_{t=\tau_s} \tag{48}$$

doi: 10.1049/iet-rsn.2013.0169

Application of (45)–(48) into (43) and (44) gives

$$x(\tau_s) = \bar{\alpha}_0 - \frac{\bar{\beta}_1}{\kappa_0}\tau_s^2 \tag{49}$$

$$y(\tau_s) = \{\bar{\beta}_0 + \kappa_0\bar{\alpha}_1\} + 2\bar{\beta}_1\tau_s \tag{50}$$

The parametric specification of the smear signature in (49) and (50) traces the form a parabola wherein the centre of the smear is offset in the ground cross-range direction from the mean value of the true target location by the distance $\kappa_0\bar{\alpha}_1$. Thus, the magnitude of this ground cross-range offset is directly proportional to the ground down-range component of the target velocity. The magnitude of this offset, which determines whether the signature smear is offset to the right or to the left of the true target location, depends upon the sign of the product $\kappa_0\bar{\alpha}_1$. The sign of this product, in turn, depends upon whether the target is moving towards or away from the radar and whether the radar platform is pointing the radar beam to the starboard side or to the port side.

Equations (49) and (50) also reveal that the extent of the smear is governed primarily by the term in $y(\tau_s)$ that is linear in τ_s, which is directly proportional to the ground cross-range component of the target velocity $\bar{\beta}_1$. The sign of this ground cross-range target velocity component $\bar{\beta}_1$ determines whether the smear drifts to the left or the right when sequencing forward in various subapertures characterised by mean time τ_s. If the target cross-range velocity component $\bar{\beta}_1$ is exactly zero, then there is no signature smearing. Instead, the target appears focused as if it were exactly stationary, but displaced from its true location in the cross-range direction by a distance $\kappa_0\bar{\alpha}_1$ for a target with a non-zero down-range velocity component.

The sign of $\bar{\beta}_1$ also affects whether the parabolic smear shape is either concave up or concave down as determined by the quadratic term in τ_s in (49). Again, the basic condition for the necessity of this 2D smearing analysis is that the smearing must cover an extent in the down-range direction that exceeds a single pixel cell in the down-range direction. Specifically, the 2D smearing analysis described herein is required for constant velocity targets for cases in which the down-range resolution δx is less than the magnitude of the second term in (49), that is

$$\delta x < \left|\frac{\bar{\beta}_1}{\kappa_0}\tau_s^2\right| \tag{51}$$

5.2 Constant acceleration targets

The next special case to be examined is that of a target moving with constant acceleration, that is

$$\alpha(t) = \bar{\alpha}_0 + \bar{\alpha}_1 t + \frac{1}{2}\bar{\alpha}_2 t^2 \tag{52}$$

$$\beta(t) = \bar{\beta}_0 + \bar{\beta}_1 t + \frac{1}{2}\bar{\beta}_2 t^2 \tag{53}$$

with $\bar{\alpha}_0$, $\bar{\alpha}_1$, $\bar{\beta}_0$, $\bar{\beta}_1$, $\bar{\alpha}_2$ and $\bar{\beta}_2$ all constant parameters. Use of (47), (48), (52) and (53) in (43) and (44) yields

$$x(\tau_s) = \bar{\alpha}_0 - \left\{\frac{\bar{\beta}_1}{\kappa_0} + \frac{\bar{\alpha}_2}{2}\right\}\tau_s^2 - \frac{\bar{\beta}_2}{\kappa_0}\tau_s^3 \tag{54}$$

$$y(\tau_s) = \{\bar{\beta}_0 + \kappa_0\bar{\alpha}_1\} + \{2\bar{\beta}_1 + \kappa_0\bar{\alpha}_2\}\tau_s + \frac{3}{2}\bar{\beta}_2\tau_s^3 \tag{55}$$

Examination of (54) and (55) shows that the mean value of the ground cross-range location of the smear is offset from the true value of the mean target location by the distance $\kappa_0\bar{\alpha}_1$, as occurs for the constant velocity case in (50). However, (55) shows that an additional term proportional to the ground down-range component of the true target acceleration, that is, $\bar{\alpha}_2$, now modifies the cross-range extent of the smear. This sign of this additional term can be positive or negative, so that it can serve either to increase or decrease the smear extent over that because of the ground cross-range velocity component alone, that is, $\bar{\beta}_1$. This same combination of ground cross-range velocity and ground down-range acceleration, that is, $2\bar{\beta}_2 + \kappa_0\bar{\alpha}_2$ also determines whether the parabolic part of the smear signature, as determined by the second-order term in (54) is either concave up or concave down. The parametric structure of the smear for this case of constant target acceleration also contains third-order terms that are proportional to the ground cross-range component of the target acceleration.

5.3 Constant turning radius targets

The case of the previous subsection for a target moving with constant acceleration can yield a turning target if the constant acceleration vector is approximately perpendicular to the direction of motion. The next special case to be examined is that of a constant turning target, which is defined to have both constant speed and a constant turning radius, that is

$$\alpha(t) = \bar{\alpha}_0 \mp \bar{\rho}_0\sin(\bar{\phi}_0) \pm \bar{\rho}_0\sin\left(\pm\frac{\bar{v}_0 t}{\bar{\rho}_0} + \bar{\phi}_0\right) \tag{56}$$

$$\beta(t) = \bar{\beta}_0 \pm \bar{\rho}_0\cos(\bar{\phi}_0) \mp \bar{\rho}_0\cos\left(\pm\frac{\bar{v}_0 t}{\bar{\rho}_0} + \bar{\phi}_0\right) \tag{57}$$

with $\bar{\alpha}_0$, $\bar{\beta}_0$, $\bar{v}_0$, $\bar{\rho}_0$ and $\bar{\phi}_0$ all constant parameters. Use of (47), (48), (56) and (57) in (43) and (44) yields

$$x(\tau_s) = \bar{\alpha}_0 \mp \bar{\rho}_0\sin(\bar{\phi}_0) \pm \{\bar{\rho}_0 \mp \varepsilon_s^2\kappa_0\bar{v}_0\} \sin\left(\pm\frac{\bar{v}_0\tau}{\bar{\rho}_0} + \bar{\phi}_0\right) - \varepsilon_s\kappa_0\bar{v}_0\cos\left(\pm\frac{\bar{v}_0\tau}{\bar{\rho}_0} + \bar{\phi}_0\right) \tag{58}$$

$$y(\tau_s) = \bar{\beta}_0 \pm \bar{\rho}_0\cos(\bar{\phi}_0) \mp \{\bar{\rho}_0 \mp \kappa_0\bar{v}_0\} \cos\left(\pm\frac{\bar{v}_0\tau}{\bar{\rho}_0} + \bar{\phi}_0\right) + \varepsilon_s\kappa_0\bar{v}_0\sin\left(\pm\frac{\bar{v}_0\tau}{\bar{\rho}_0} + \bar{\phi}_0\right) \tag{59}$$

This case of a target with a constant speed and a constant turning radius is similar to a target with constant acceleration for which the direction of acceleration is perpendicular to the direction of motion. Thus, such a constant turning target is expected to have some smear components that are because of target velocity and others because of target acceleration, which can be additive or subtractive in the overall smear extent and concavity.

5.4 Hyperbolic tangent speed targets

An interesting special case is obtained corresponding to a target that moves with constant heading according to a hyperbolic tangent speed profile, that is, $\tanh(t)$. The

integral of this speed profile yields a position profile that is proportional to ln(cosh(*t*)). Thus, the following true target trajectory is considered

$$\alpha(t) = \bar{\alpha}_0 + \cos(\bar{\phi}_0)\left\{\bar{v}_0 t + \bar{w}_0\bar{\gamma}_0 \ln\left(\cosh\left(\frac{t-\bar{t}_0}{\bar{\gamma}_0}\right)\right)\right\} \quad (60)$$

$$\beta(t) = \bar{\beta}_0 + \sin(\bar{\phi}_0)\left\{\bar{v}_0 t + \bar{w}_0\bar{\gamma}_0 \ln\left(\cosh\left(\frac{t-\bar{t}_0}{\bar{\gamma}_0}\right)\right)\right\} \quad (61)$$

in terms of the parameters $\{\bar{\alpha}_0, \bar{\beta}_0, \bar{v}_0, \bar{w}_0, \bar{\gamma}_0, \bar{\phi}_0, \bar{t}_0\}$. The resulting target speed profile has the simple analytic form

$$\sqrt{\left[\frac{\mathrm{d}\alpha}{\mathrm{d}t}\right]^2 + \left[\frac{\mathrm{d}\beta}{\mathrm{d}t}\right]^2} = \bar{v}_0 + \bar{w}_0 \tanh\left(\frac{t-\bar{t}_0}{\bar{\gamma}_0}\right) \quad (62)$$

which models a target that transitions from one speed to another. Based upon (60) and (61), (43) and (44) give

$$\begin{aligned} x(\tau_s) = {} & \bar{\alpha}_0 - \tau_s^2 \sin\left(\bar{\phi}_0\right)\frac{\bar{v}_0}{\kappa_0} \\ & + \cos\left(\bar{\phi}_0\right)\bar{w}_0\bar{\gamma}_0 \ln\left(\cosh\left(\frac{\tau_s-\bar{t}_0}{\bar{\gamma}_0}\right)\right) \\ & - \tau_s\bar{w}_0\left\{\cos\left(\bar{\phi}_0\right) + \frac{\tau_s}{\kappa_0}\sin\left(\bar{\phi}_0\right)\right\}\tanh\left(\frac{\tau_s-\bar{t}_0}{\bar{\gamma}_0}\right) \end{aligned} \quad (63)$$

$$\begin{aligned} y(\tau_s) = {} & \bar{\beta}_0 + \bar{v}_0\left\{\kappa_0\cos\left(\bar{\phi}_0\right) + \tau_s\sin\left(\bar{\phi}_0\right)\right\} \\ & + \sin\left(\bar{\phi}_0\right)\left\{\bar{v}_0\tau_s + \bar{w}_0\bar{\gamma}_0\ln\left(\cosh\left(\frac{\tau_s-\bar{t}_0}{\bar{\gamma}_0}\right)\right)\right\} \\ & + \bar{w}_0\left\{\kappa_0\cos\left(\bar{\phi}_0\right) + \tau_s\sin\left(\bar{\phi}_0\right)\right\}\tanh\left(\frac{\tau_s-\bar{t}_0}{\bar{\gamma}_0}\right) \end{aligned} \quad (64)$$

Understanding and interpretation of (63) and (64) will be examined in the next section.

6 SAR signature results

The equations above in Sections 2 and 3 are used to generate simulated smear signatures for moving targets within spotlight SAR imagery. The radar platform for the scenario below is assumed to be imaging with broadside geometry and a constant and level flight path. The selected trajectory parameters of (3)–(5) for this notional radar platform are a speed of $V_0 = 200$ m/s, a ground range of $X_0 = 30$ km and an elevation of $Z_0 = 1$ km. A total of 1100 radar waveforms with a radar centre frequency of $f_c = 1.5$ GHz are transmitted and received at uniform intervals over a total synthetic aperture time of $T_0 = 15$ s. The radar bandwidth is 0.15 GHz, and the signal processor collects complex I and Q data over 700 samples distributed for each radar waveform, distributed uniformly over the radar bandwidth.

6.1 Constant velocity targets

The first example considers the case in which the radar mainbeam is assumed to be pointed off of the left (i.e. port) side of the platform. Thus, the radar effectively moves along the top of the image from the right towards the left direction (i.e. in the negative cross-range direction $-y$), as given by the minus sign of the $\pm$ in (4). Fig. 1*a* shows the spotlight-SAR signature resulting from one point target that is moving with constant velocity. The midpoint spatial position is given by $\{\bar{\alpha}_0 = 0.0\ \mathrm{m}\}$ and $\{\bar{\beta}_0 = 0.0\ \mathrm{m}\}$ at the midpoint time of $t = 0$ s. The target velocity is given by the parameter values $\{\bar{\alpha}_1 = 1.455\ \mathrm{m/s}\}$, and $\{\bar{\beta}_1 = -9.509\ \mathrm{m/s}\}$, corresponding to a speed of 9.62 m/s and a heading of $-81.3°$ relative to the radar down-range direction. Thus, the target is primarily moving in the $-y$ cross-range direction. The spotlight SAR image of Fig. 1*a* shows that the resulting signature lies primarily in the horizontal direction, which corresponds to the radar cross-range direction.

There is a slight downward bowing of the signature in the spotlight SAR image of Fig. 1*a*.This bowing effect is more evident in the smaller image chip of Fig. 1*b*, wherein the down-range image axis has been stretched relative to the cross-range image axis in order to facilitate examination of the target migration effects. Such an unequal selection of image axes are used in the remainder of the SAR image plots, again to provide a visual aid into the SAR moving target phenomenology.

In Fig. 1*b* and each of the following SAR image chips, unweighted apertures are used in both the down-range and cross-range spatial frequency directions. Of course, weighting functions can be applied to make the signature smears have a smoother appearance. In addition, the image pixel sampling in both the down-range and cross-range spatial directions are selected to correspond exactly to the corresponding pixel resolutions in both dimensions. That is, no zero padding has been applied in the spatial frequency domain in order to provide for a more pleasing signature. The choice to avoid the use of weighting function and zero padding was made so that the reader can see the basic effects of target migration in the smear signatures.

Equations (49) and (50) give the predicted parametric trajectory for a constant velocity target within a spotlight SAR image. These equations are used to generate the parametric trajectory of Fig. 1*c* corresponding to the constant velocity target of Fig. 1*b*, showing excellent agreement of the predictive theory with the SAR signature. The coordinate values of the down-range $\{x\}$ and cross-range $\{y\}$ axes are correct in both the predictive image of Fig. 1*b* and in the SAR signature of Fig. 1*b*. Therefore this analysis reveals that accurate signature predictions have been obtained for both the cross-range positional offset of the signature relative to its true position and for the shape and extent of the resulting smear signature.

The next example of Fig. 2 considers the exact same constant velocity target, but with the radar mainbeam pointed off of the right (i.e. starboard) side. Thus, the radar effectively moves along the top of the image from the left towards the right direction (i.e. in the positive cross-range direction $+y$), as given by the plus sign of the $\pm$ in (4). This reversal of the radar platform direction yields an opposite direction for the cross-range offset of the SAR smear relative to the true target location. In addition, the radar direction reversal also yields a reversal in the sign of the concavity of the smear bowing effect for this constant velocity target.

Notice that the reversal of the radar platform direction implies that the constant κ_0 of (20) changes sign. Thus, the $\kappa_0\bar{\alpha}_1$ term of (50) predicts that the cross-range offset changes direction under the reversal of the radar direction.

doi: 10.1049/iet-rsn.2013.0169

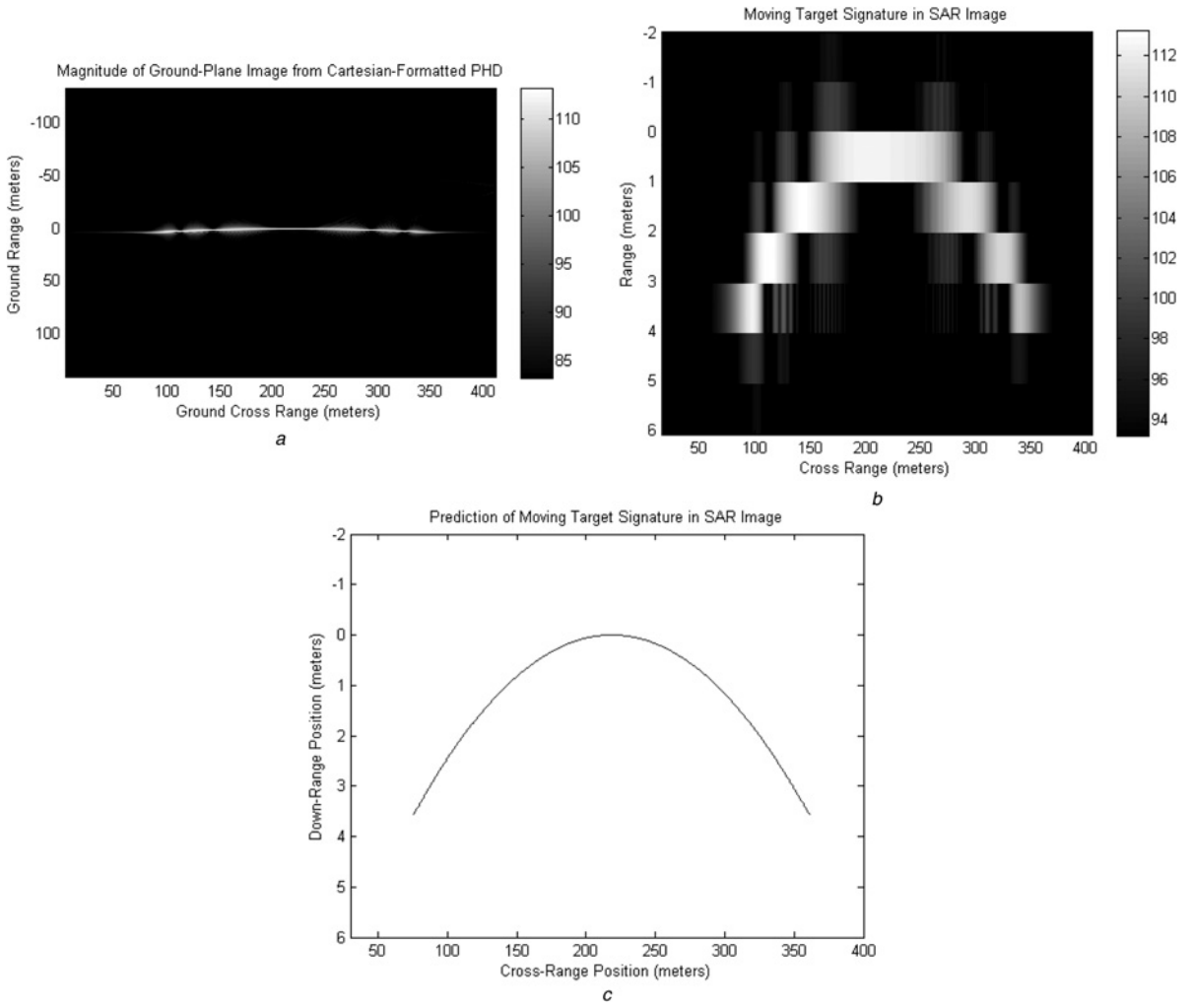

Fig. 1 *Constant velocity target for the case of a leftward pointing radar mainbeam*

a Moving target signature in spotlight SAR imagery
b Image zoom of this same moving target signature
c Corresponding predicted signature based upon the true target motion

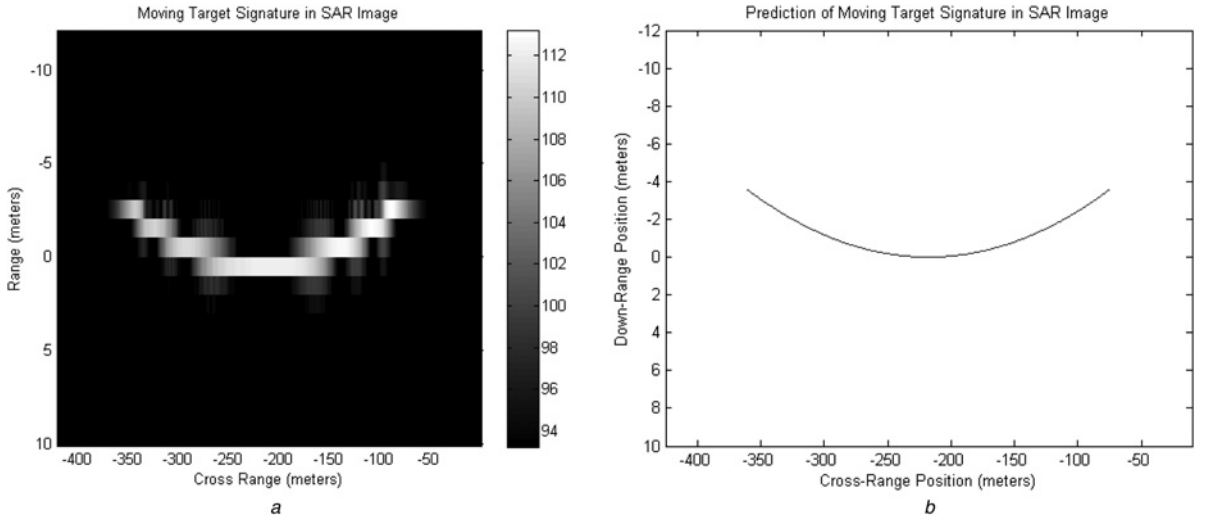

Fig. 2 *Constant velocity target for the case of rightward pointing radar mainbeam*

a Image zoom of moving target signature in spotlight SAR imagery
b Corresponding predicted signature based upon the true target motion

Furthermore, the $-\bar{\beta}_1 \tau_s^2/\kappa_0$ term of (49) predicts the reversal in the sign of the smear bowing concavity with the reversal of the radar direction. These results are upheld in the predictive signature plot of Fig. 1, which gives accurate agreement in the overall smear position, extent and concavity with SAR signature of Fig. 1. A discussion of this target migration effect for constant velocity targets in stripmap SAR imagery was presented by Jao [24].

6.2 Constant turning targets

The next set of examples are based upon the same radar platform motions as given previously, but with a target that is moving with constant speed and a constant turning radius. The specific example has a very large turning radius and is selected to be moving with the same speed and the same average heading as with the constant velocity target given above. The particular parameters values selected are given by $\{\bar{\alpha}_0 = 0.0 \text{ m}\}$, $\{\bar{\beta}_0 = 0.0 \text{ m}\}$, $\{\bar{v}_0 = 9.62 \text{ m/s}\}$, $\{\bar{\rho}_0 = 500.0 \text{ m}\}$ and $\{\bar{\phi}_0 = -81.3^\circ\}$. Fig. 3*a* shows the resulting SAR smear signature for the case of a radar mainbeam that is pointed off of the port side, corresponding to a minus sign of the $\pm$ in (4).

Equations (58) and (59) give the predicted parametric trajectory for a constant turning target within a spotlight SAR image. These equations are used to generate the parametric trajectory of Fig. 3*b* corresponding to the constant turning target of Fig. 3, again revealing excellent agreement of the predictive theory with the numerical SAR signature. Again, the coordinate values of the down-range $\{x\}$ and cross-range $\{y\}$ axes are correct in both the predictive image of Fig. 3*a* and the SAR signature of Fig. 3*b*. Thus, accurate predictive behaviour has been obtained for both the cross-range positional offset of the signature relative to its true position and for the shape and extent of the resulting smear signature.

It is interesting that the gentle turn of a very large radius of curvature of 0.5 km over a 15 s collection time is sufficient to yield a concavity direction in Figs. 3*a* and *b* that is exactly opposite to that of an exactly constant velocity target with the same speed and average direction, as given by Figs. 1*a* and *b*. An understanding of this effect is evident in examining the quadratic term in τ_s for the down-range component of the predictive signature of (54) for a target moving with constant acceleration. Again, the constant turning target is approximately characterised by a constant acceleration target in which the direction of acceleration is perpendicular to the direction of motion. In particular, the quadratic term of (54) has two contributions: one proportional to the cross-range component of the target velocity, that is, $\bar{\beta}_1/\kappa_0$, and the other proportional to the down-range component of the target acceleration, that is, $\bar{\alpha}_2/2$. These two components have a different dependence upon the radar platform direction, as encompassed by κ_0 of (20). Thus, these contributions can be additive or subtractive. For this case, the two contributions are subtractive, and the additional acceleration term is larger in magnitude than the original velocity term of the constant velocity case.

Figs. 4*a* and *b* give the SAR mover signature and the predictive smear trajectory for the same constant turning target for the case in which the radar mainbeam is pointed in the opposite direction, that is, off of the starboard side of the radar platform. Again, these plots show excellent agreement in terms of the position, extent, and concavity of the smear. In fact, this smear has a greater extent and the same concavity in comparison to the constant velocity case of Figs. 2*a* and *b*, which are characterised by a target with the same speed and approximate heading. For this case, the contributions because of the cross-range velocity and the down-range acceleration are additive within the down-range component of the prediction signature of (54) for the corresponding approximate constant acceleration case. In addition, the cross-range component of the predictive signature of (55) has these same two contributions to the linear term in τ_s, so that the cross-range extent of the smear has increased as well.

6.3 Hyperbolic tangent speed targets

This subsection attempts to utilise the hyperbolic tangent speed profile provided in (60)–(61). The corresponding true target speed profile is given by (62) and shown in Fig. 5*a*. The particular parameter values selected are given by $\{\bar{\alpha}_0 = 0.0 \text{ m}\}$, $\{\bar{\beta}_0 = 0.0 \text{ m}\}$, $\{\bar{v}_0 = 9.62 \text{ m/s}\}$, $\{\bar{w}_0 = -4.13 \text{ m/s}\}$, $\{\bar{\gamma}_0 = 0.5 \text{ s}\}$ and $\{\bar{\phi}_0 = -81.3^\circ\}$.

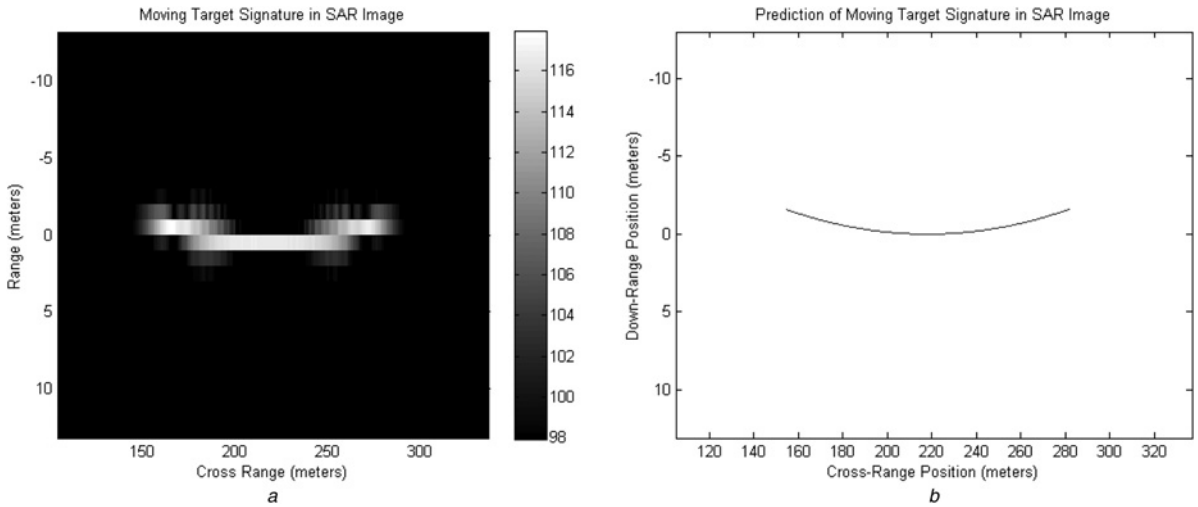

Fig. 3 *Constant turning target for the case of leftward pointing radar mainbeam*

a Image zoom of moving target signature in spotlight SAR imagery
b Corresponding predicted signature based upon the true target motion

doi: 10.1049/iet-rsn.2013.0169

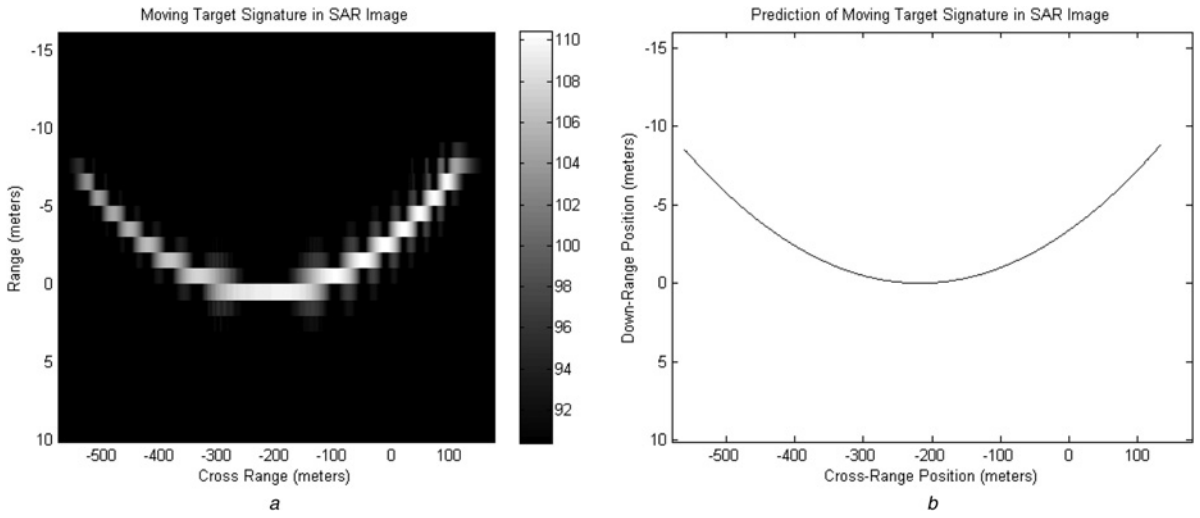

Fig. 4 *Constant turning target for the case of rightward pointing radar mainbeam*

a Image zoom of moving target signature in spotlight SAR imagery
b Corresponding predicted signature based upon the true target motion

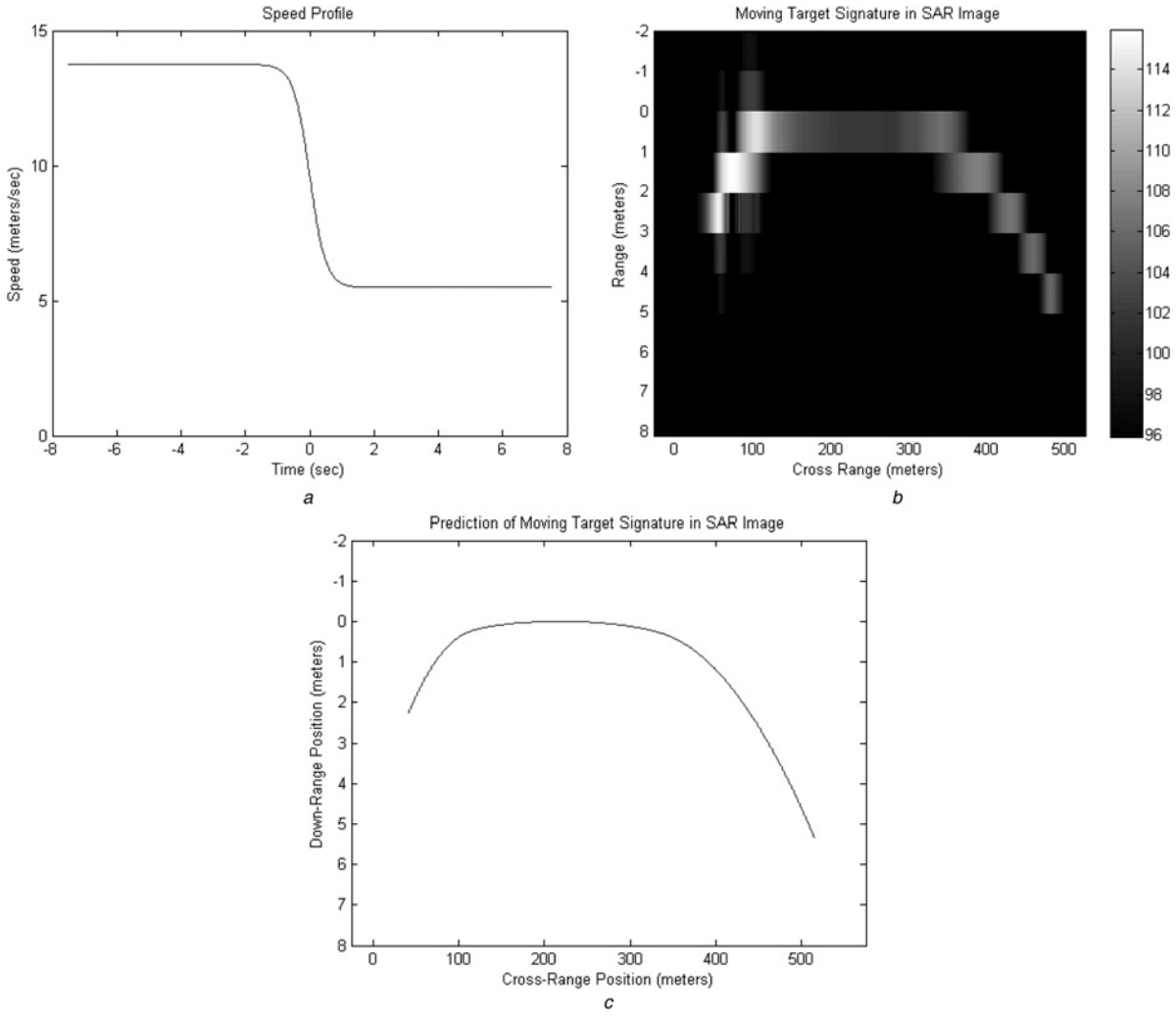

Fig. 5 *Hyperbolic tangent speed target for the case of leftward pointing radar mainbeam*

a Speed profile for a target that is moving according to a braking manoeuvre via a hyperbolic tangent speed function
b Image zoom of moving target signature in spotlight SAR imagery
c Corresponding predicted signature based upon the true target motion

This selection of the target motion parameters corresponds to the realistic scenario of a target that is initially traveling with approximately constant speed and heading but encounters circumstances that cause the target to undergo a rapid deceleration (i.e. a braking manoeuvre) to a slower approximately constant speed and the same heading.

Of course, most targets move with constant velocity and acceleration, at least for relatively small SAR collection time intervals on the order of a second. For longer SAR collection times, more complicated target trajectories are possible – thus motivating the present analysis herein. In addition, targets that slow from one speed to another during the SAR collection interval exhibit a hyperbolic tangent speed. Such targets are more common in an urban environment than on open roads. Furthermore, the use of the hyperbolic tangent speed target illuminates the robustness of the theory presented herein. Specifically, the fidelity of the match between the predicted and actual signatures of Figs. 5*b* and *c*, coupled with the complicated expressions for the true hyperbolic tangent speed target trajectory of (60) and (61) and the resulting signature of (63) and (64), further validates the general signature prediction (43) and (44).

The collection parameters for the radar platform are the same as with the earlier examples. Fig. 5*b* shows the resulting SAR smear signature for the case of a radar mainbeam that is pointed off of the left side, corresponding to a minus sign of the $\pm$ in (4). This smear signature clearly does not have the simple symmetrical bowing shape of any of the previous examples obtained from constant velocity or constant turning targets. The smear signature seems to have a non-uniform curvature along its trajectory.

Equations (63) and (64) give the predicted parametric trajectory for this target moving with a hyperbolic tangent speed profile and a constant heading. These equations are used to generate the parametric trajectory of Fig. 5*c* corresponding to the hyperbolic tangent speed target of Fig. 5*b*. These results yield excellent agreement between the predictive smear trajectory and the numerical SAR signature. In particular, both the down-range $\{x\}$ and cross-range $\{y\}$ component of the parametric smear trajectory via (63) and (64) reveals an accurate predictive capability for the resulting SAR smear signature.

Figs. 6*a* and *b* give the SAR mover signature and the predictive smear trajectory for the same hyperbolic tangent speed target for the case in which the radar mainbeam is

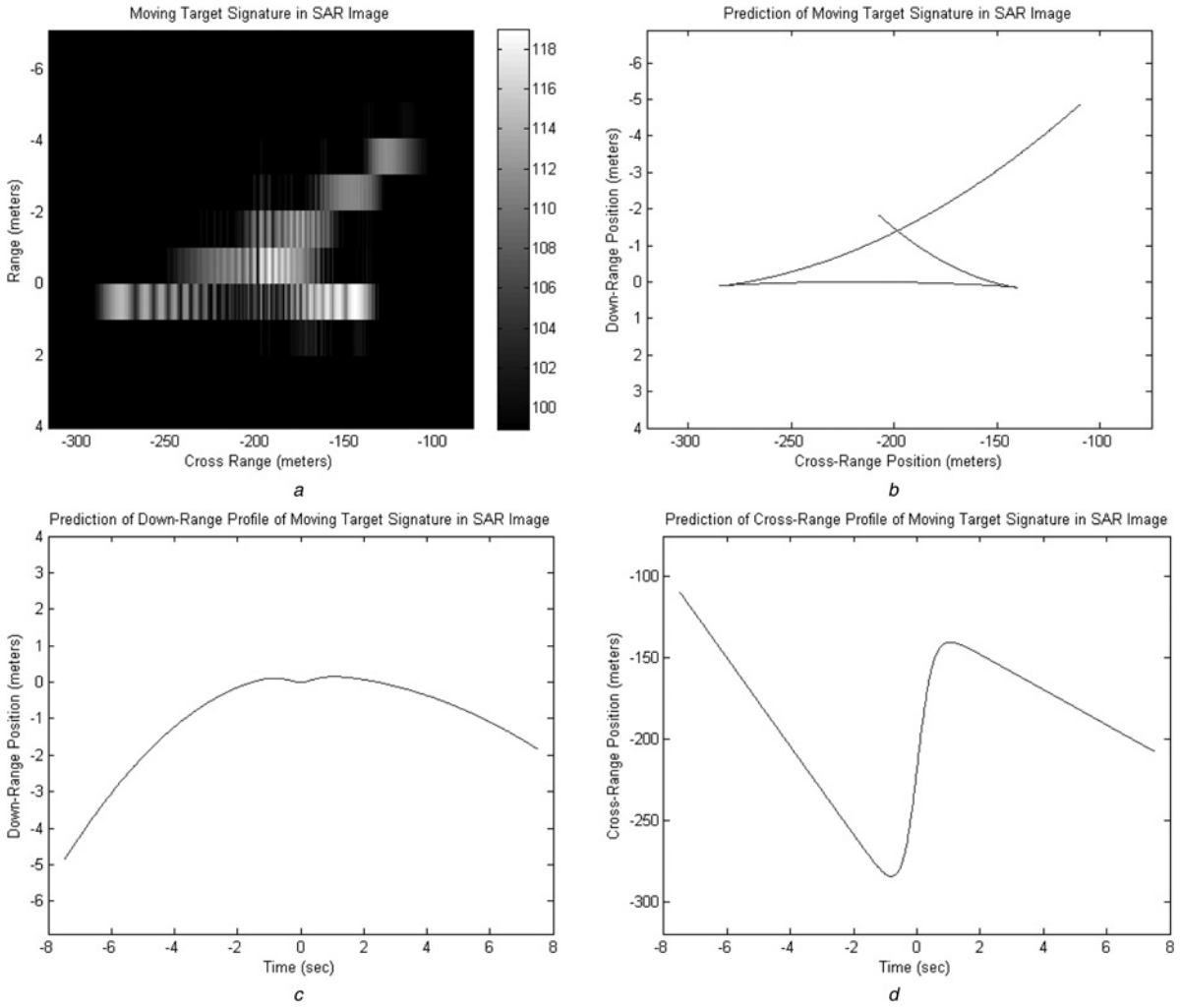

Fig. 6 *Hyperbolic tangent speed target for the case of rightward pointing radar mainbeam*

a Image zoom of moving target signature in spotlight SAR imagery
b Corresponding predicted signature based upon the true target motion
c Down-range component of the predicted signature – note that positive down-range points up in this 1D predictive parametric plot, whereas positive down-range points down in all of the previous 2D predictive parametric plots and in the SAR signature plots
d Cross-range component of the predicted signature

doi: 10.1049/iet-rsn.2013.0169

pointed off of the starboard side of the radar platform. As with the previous examples, there is excellent agreement between the SAR signature itself and the predictive smear trajectory, in terms of overall smear position, extent and shape. This particular case yields an especially interesting signature in that the smear trajectory seems to cross back upon itself. Both the SAR signature itself of Fig. 6*a* and the predictive smear trajectory of Fig. 6*b* seems to support this prediction. An examination of the predictive parametric smear trajectories, as shown in Figs. 6*c* and *d*, details the manner in which the subaperture trajectory cross back onto itself. In particular, the cross-range component travels in the $-y$ direction initially, then travels in the $+y$ during the middle of the SAR collection, and finally again travels in the $-y$ direction. These unusually shaped SAR moving target signatures deviate significantly from the earlier examples that gave relatively symmetrical bowing signatures.

7 Conclusions

This analysis has examined the effects of range migration signatures for moving targets within spotlight-SAR imagery. The techniques developed herein give a single predictive set of parametric equations for the radar down-range and cross-range components of the smear signature within the SAR image data. Constant velocity targets were shown to give bowed smear shapes that are consistent with earlier studies of moving-target smear phenomenology [24]. In fact, there seems to be a perception that all target smear signatures have the simple bowing shape of a parabola or a hyperbola that has been shown for constant velocity targets. The detailed analysis of range migration for focusing stationary scenes via lower frequency radar enhances the perception of simply curved bowing signatures for the analysed effects. However, the analysis given in the current paper reveals that more complicated shapes are possible.

The predictive equations describing the SAR smear signature resulting from a particular motion offers the potential capability of characterising true target motion based upon the SAR smear signature alone. For example, simply curved smear signatures only seem to result for the case of constant-velocity targets. Thus, it a more complicated smear signature is observed, as with Figs. 5*b* or 6*a*, then one can conclude that the target causing this smear is not moving with constant velocity. Further investigation of the predictive equations for the smear signature shape offers more insight into true target motion characteristics.

The validation of these results with regards to real examples collected with actual measured SAR data is reserved for future work. Additional complications can arise since real targets are comprised of many inhomogeneous scattering centres with different individual velocities. In addition, there can be other corrections for a radar platform trajectory that does not follow a straight line trajectory. Finally, it is possible that the theory developed herein can be used in forming focused images of extended targets moving with complex motion.

8 Acknowledgments

The author would like to thank the referees for valuable suggestions. DoD Distribution Statement A: Unlimited Distribution. The views expressed in this document are those of the author and do not reect the offcial policy or position of the Department of Defense or the U.S. Government.

9 References

1 Raney, R.K.: 'Synthetic aperture imaging radar and moving targets', *IEEE Trans. Aerosp. Electron. Syst.*, 1971, **7**, pp. 499–505
2 Perry, R.P., DiPietro, R.C., Fante, R.L.: 'SAR imaging of moving targets', *IEEE Trans. Aerosp. Electron. Syst.*, 1999, **35**, pp. 188–200
3 Fienup, J.R.: 'Detecting moving targets in SAR imagery by focusing', *IEEE Trans. Aerosp. Electron. Syst.*, 2001, **37**, pp. 794–809
4 Cristallini, D., Pastina, D., Colone, F., Lombardo, P.: 'Efficient detection and imaging of moving targets in SAR images based on chirp scaling', *IEEE Trans. Geosci. Reomote Sens.*, 2013, **51**, pp. 2403–2416
5 Jakowatz Jr., C.V., Wahl, D.E., Eichel, P.H.: 'Refocus of constant velocity moving targets in synthetic aperture radar imagery'. Proc. SPIE: Algorithms for Synthetic Aperture Radar Imagery V, 1998, 3370, pp. 85–95
6 Rigling, B.D.: 'Image-quality focusing of rotating SAR targets', *IEEE Geosci. Remote Sens. Lett.*, 2008, **5**, pp. 750–754
7 Vu, V.T.S., Pettersson, T.K., Gustavsson, M.I., Ulander, A., Lars, M.H.: 'Detection of moving targets by focusing in UWB SAR – theory and experimental results', *IEEE Trans. Geosci. Remote Sens.*, 2010, **48**, (10), pp. 3799
8 Stojanovic, I., Karl, W.C.: 'Imaging of moving targets with multi-static SAR using an over complete dictionary', *IEEE J. Sel. Top. Signal Process.*, 2010, **4**, pp. 164–176
9 Leducq, P., Ferro-Famil, L., Pottier, E.: 'Matching-pursuit-based analysis of moving objects in polarimetric SAR images', *IEEE Geosci. Remote Sens. Lett.*, 2008, **5**, pp. 123–127
10 Fasih, A.R., Emre Ertin, J.N.A.R.L.M.: 'SAR focusing performance for moving objects with random motion components'. Proc. 42nd Asilomar Conf. Signals, Systems and Computers, 2008 (ACSSC 08), October 2008, 2008, pp. 1628–1632
11 Zhu, S., Liao, G., Qu, Y., Zhou, Z., Liu, X.: 'Ground moving targets imaging algorithm for synthetic aperture radar', *IEEE Trans. Geosci. Remote Sens.*, 2011, **49**, pp. 462–477
12 Cheney, M., Borden, B.: 'Waveform-diverse moving-target spotlight SAR'. Proc. 2010 Int. Waveform Diversity and Design Conf., Niagara Falls, 8–13 August 2010, Canada, pp. 33–34
13 Xu, J., Zuo, Y., Xia, B., Xia, X.-G., Peng, Y.-N., Wang, Y.-L.: 'Ground moving target signal analysis in complex image domain for multichannel SAR', *IEEE Trans. Geosci. Remote Sens.*, 2012, **50**, pp. 538–552
14 Yake, L., Yanfei, W., Chang, L.: 'Detect and autofocus the moving target by its range walk in time domain'. IEEE, 2011
15 Li, X., Deng, B., Qin, Y., Wang, H., Li, Y.: 'The influence of target micromotion on SAR and GMTI', *IEEE Trans. Geosci. Remote Sens.*, 2011, **49**, pp. 2738–2751
16 Deng, B., Qin, Y., Wang, H., Li, X.: 'An efficient mathematical description of range models for high order-motion targets in synthetic aperture radar'. Proc. 2012 IEEE Radar Conf., Atlanta, Georgia, 7–11 May 2012, pp. 6–10
17 DiPietro, R.C., Fante, R.L., Perry, R.P.: 'Space-based bistatic GMTI using low resolution SAR'. IEEE Aerospace Conf., 1997, vol. 2, pp. 181–193
18 Barbarossa, S., Farina, A.: 'A novel procedure for detecting and focusing moving objects with SAR based on the Wigner-Ville distribution'. IEEE Int. Radar Conf., 1990, pp. 44
19 Barbarossa, S.: 'Detection and imaging of moving objects with synthetic aperture radar – Part 1: optimal detection and parameter estimation theory', *IEE Proc. F*, 1992, **139**, pp. 79–88
20 Barbarossa, S., Farina, A.: 'Detection and imaging of moving objects with synthetic aperture radar – Part 2: joint time–frequency analysis by Wigner-Ville distribution', *IEE Proc. F*, 1992, **139**, pp. 89–97
21 Kirscht, M.: 'Detection and imaging of arbitrarily moving targets with single-channel SAR', *IEE Proc. Radar Sonar Navig.*, 2003, **150**, pp. 7–11
22 Dias, J.M.B., Marques, P.A.C.: 'Multiple moving target detection and trajectory estimation using a single SAR sensor', *IEEE Trans. Aerosp. Electron. Syst.*, 2003, **39**, pp. 604–624
23 Marques, P.A.C., Dias, J.M.B.: 'Moving targets processing in SAR spatial domain', *IEEE Trans. Aerosp. Electron. Syst.*, 2007, **43**, pp. 864–874
24 Jao, J.K.: 'Theory of synthetic aperture radar imaging of a moving target', *IEEE Trans. Geosci. Remote Sens.*, 2001, **39**, pp. 1984–1992
25 Stolt, R.H.: 'Migration by Fourier transform', *Geophysics*, 1978, **43**, pp. 23–48

26 Rahman, S.: 'Focusing moving targets using range migration algorithm in ultra wideband low frequency synthetic aperture radar', Master's thesis, Blekinge Institue of Technology, 2010

27 Garren, D.A.: 'Method and system for developing and using an image reconstruction algorithm for detecting and imaging moving targets', U.S. Patent 7,456,780 B1, Issued: 25 November 2008, November 2008

28 Mao, X.Z., Zhu, Z.-D.D.-Y.: 'Signatures of moving target in polar format spotlight SAR image', *Prog. Electromagn. Res.*, 2009, **92**, pp. 47–64

29 Mao, X., Zhu, D., Wang, L., Zhu, Z.: 'Response of polar format algorithm to moving target with consideration of wavefront curvature'. IEEE Radar Conf., Pasadena, CA, 2009

30 Linnehan, R., Perlovsky, L., Mutz, C., Schindler, J.: 'Detecting slow moving targets in SAR images'. Proc. SPIE 5410, Radar Sensor Technology VIII and Passive Millimeter-Wave Imaging Technology VII, 12 August 2004, vol. 64

31 Garren, D., Scrofani, J.W., Tummala, M., McEachen, J.C.: 'Target migration path morphology of moving targets in spotlight sar'. To appear in 'Algorithms for Synthetic Aperture Radar Imagery XX' of the SPIE Defense, Security, and Sensing Conf., Baltimore, Maryland, USA, 29 April–3 May 2013

32 Munson Jr., D.C., O'Brien, J.D., Jenkins, W.K.: 'A tomographic formulation of spotlight-mode synthetic aperture radar', *Proc. IEEE*, 1983, **71**, (8), pp. 917–925

33 Webb, J.L.H., Munson Jr., D.C.: 'SAR image reconstruction for an arbitrary radar path'. Proc. 1995 Int. Conf. Acoustics, Speech, and Signal Processing Detroit, MI, 9–12 May 1995, vol. 4, pp. 2285–2288

34 Carrara, W.G., Goodman, R.S., Majewski, R.M.: 'Spotlight synthetic aperture radar signal pro-cessing algorithms' (Artech House, Norwood, MA, USA, 1995)

35 Jakowatz Jr., C.V., Wahl, D.E., Eichel, P.H., Ghiglia, D.C., A. Thompson, P.: 'Spotlight-mode synthetic aperture radar: a signal processing approach' (Kluwer Academic Publishers, Norwell, MA, USA, 1996)

36 Xiao, S., Munson Jr., D.C.: 'Spotlight-mode SAR imaging of a three-dimensional scence using spectral estimation techniques'. Proc. 1998 IEEE Int. Geoscience and Remote Sensing Symp. (IGARSS '98), 1998, vo*l*. **2**, pp. 642–644

37 Perry, R.P., DiPietro, R.C., Johnson, B.L., Kozma, A., Vaccaro, J.J.: 'Planar subarray processing for SAR imaging'. IEEE Int. Radar Conf., 1995, pp. 473–478

38 Zhang, J., Xu, J., Peng, Y., Wang, X.: 'Speckle filtering of SAR images based on sub-aperture technique and principal component analysis', IEEE Int. Symp. Communications and Information Technology 2005 (ISCIT 2005), 2005, vol. 2, pp. 1217–1222

39 Soumekh, M.: 'A system model and inversion for synthetic aperture radar imaging', *IEEE Trans. Image Process.*, 1992, **1**, pp. 64–76

40 Soumekh, M.: 'Digital spotlighting and coherent subaperture image formation for stripmap synthetic aperture radar'. Proc. IEEE Int. Conf. Image Processing, 1994 (ICIP-94), 1994, vol. 1, pp. 476–480

41 Ferro-Famil, L., Reigber, A., Pottier, E., Boerner, W.-M.: 'Scene characterization using subaperture polarimetric SAR data', *IEEE Trans. Geosci. Remote Sens.*, 2003, **41**, pp. 2264–2276

42 Greidanus, H.: 'Sub-aperture behavior of SAR signatures of ships'. Audio, Transactions of the IRE Profession, 2006, pp. 794–809

doi: 10.1049/iet-rsn.2013.0169